Melting and solidification processes in a moving graphite-covered titanium surface subjected to multi-pulse laser irradiation

Bruno Courant, Jean-Jacques Hantzpergue, Stéphane Benayoun, Jean-Pierre L'huillier

Melting and solidification processes in a moving graphite-covered titanium surface subjected to multi-pulse laser irradiation

B Courant[1], J-J Hantzpergue[2], S Benayoun[2] and J-P L'Huillier[2]

[1]Laboratoire d'Application des Matériaux à la Mécanique, CRTT, Bd de l'Université,
BP 406, 44602 Saint-Nazaire Cedex, France
[2]Laboratoire Procédés - Matériaux - Instrumentation, ENSAM, 2 bd du Ronceray, BP 3525,
49035 Angers Cedex, France

Experimental results of surface melting by pulsed Nd–YAG laser irradiation of titanium covered with graphite powder were analysed in comparison with the results of numerical simulations. The simulations of the thermal events, such as the maximum of temperature gradient at the surface and the duration of the liquid state after irradiation, were found due to a semi-analytic model of the space–time temperature distributions which were induced by the irradiation treatments. These simulations were required in order to calculate a series of integrals by Simpson's numerical method. They have allowed us to explain the experimental results such as the incorporation of carbon in melted zone, which produces titanium carbide and possible graphite inclusions, as a function of the irradiation parameters. The perpetual absence in the thickness and the exceptional presence at the surface of the solidification structure resulting from the plane-front growth of titanium carbide have, moreover, been justified.

1. Introduction

Laser systems have been used in a number of ways to modify the properties of surfaces, especially the surfaces of metallic materials. Most often, the aim of the processing has been to harden the surface in order to provide increased wear resistance [1–3]. In some cases, the objective has been to provide improved resistance to corrosion [4–6]. Generally, such a process allows local surface treatments because of the small area receiving a high energy density. As a result, the laser beam strikes the metal surface and induces very rapid heating of a thin layer of material near the surface. When the beam moves towards a different area, the heat in the thin layer will quickly be conducted away, and the heated area cools rapidly. Compared with conventional processing technologies, such as ion or electron beams, laser processing does not require vacuum above the treated surface and allows rapid throughputs. In addition, the materials treated are varied and technological applications are numerous, such as fast surface melting and solidification, with or without surface alloying, for the steels and aluminium or titanium alloys.

Both analytical and numerical models have been the subject of numerous papers [7–14] during the last few decades. These models were developed in order to describe and quantify the thermal effects generated from the complex interaction between the metallic target and the continuous wave laser radiation. Recent articles, dealing with melting by millisecond pulsed laser irradiation are very few [15–18].

The analytical models relating the thermal effects generated by laser irradiation often refer to the work of Carlaws and Jaegger [19], which describes the heat conduction in different media. The computed solutions are based on the following simple assumptions:

(i) the thermal properties are independent of the laser beam intensity and the temperature of the solid;
(ii) surface heat losses by radiation and convection are neglected;
(iii) the latent heat of melting is not taken into account;
(iv) convection flows in the melting bath are not considered.

In some situations the laser thermal process is difficult to solve analytically; in these cases a numerical approach, based on finite difference and finite element methods, must be taken. The variations of the thermophysical properties as functions of the temperature [20–23] and, also, the convection flows in the molten bath [24–28] can be taken into account

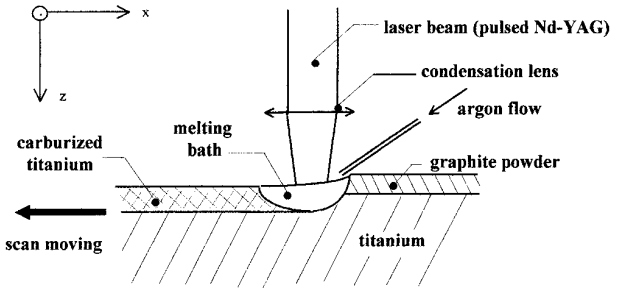

Figure 1. Schematic diagram of the experimental procedure.

by these numerical schemes. These models have been only developed for continuous wave laser beams which scan the material surface. Then, a steady state of heat transfer is reached after a transient period. The accuracy of the solution depend on the size and the number of regions used to compute the heat transfers in an iterative fashion. The disadvantage of the numerical methods is that highly-detailed models may require a significant amount of computational effort.

The theoretical investigations based on analytical or numerical procedures appear as an alternative to experimental methods, which are generally expensive and time consuming. Such simulations make the interpretation of experimental data easier and, moreover, allow one to anticipate the results. Then, the number of experiments carried out to optimize the main irradiation parameters can be reduced.

The aim of the present study was to design and to use a simulation method which describes and quantifies the thermal events resulting from the multi-pulse laser irradiation absorbed on the molten surface of titanium covered by a graphite layer (figure 1). The three-dimensional heat conduction model governs the transient heat transfer problem including a pulsed moving laser source, and takes into account the latent heat of transformation. This presents a major advantage over the above-mentioned simplified analytical models. The computed data are compared with those obtained by experimental surface melting of titanium by means of a pulsed Nd–YAG laser [29].

2. Theoretical statement

2.1. Thermal modelling

In this section we consider the sample as a semi-infinite three-dimensional solid with coordinates (x, y, z) and refer to a geometrical system with $z = 0$ at the sample surface. As depicted figure 1, the solid moves along the coordinate x at constant velocity V. The surface of this moving sample is submitted to multi-pulse laser irradiation. The problem suggests that a few assumptions are necessary in order to enable the resolution of the thermal field developed during and after the pulsed laser treatment. First, the model ignores the shielding effect of the target by a hot opaque plasma that is generated [30] and the plume of incandescent particles that extends above the surface toward the laser. Second, large pressure pulses in the target due to the absorption of the laser energy is also negligible. In fact, the regime of greatest interest for material processing applications is below the threshold for kindling of the laser supported absorption (LSA) wave (irradiance $I_0 \sim 10^7$–10^8 W cm^{-2}). Below this threshold the laser energy is mainly used for changing (melting or vaporizing) the target. Under these conditions nonlinear phenomena can be neglected, showing the possibility to estimate the induced thermal field from the basic equations of the heat transfer. Then, the heat conservation equation available for transient and three-dimensional heat transfer can be written as

$$\left(\frac{\partial}{\partial t} - \alpha\nabla^2\right)\Delta H = 0 \tag{1}$$

where α is the thermal diffusivity and ΔH is the increase of the enthalpy.

We may now consider an infinite medium where an unit quantity of heat is liberated at r' at time t' and satisfies the following differential equation:

$$\left[\frac{\partial}{\partial t} - \alpha\nabla^2\right]\Delta H = \delta(\vec{r} - \vec{r}')\delta(t - t'). \tag{2}$$

The solution takes the form

$$\Delta H(\vec{r}, t) = G(\vec{r}, \vec{r}', t, t') = \frac{1}{8[\pi\alpha(t - t')]^{3/2}} \exp\left(\frac{-(\vec{r} - \vec{r}')^2}{4\alpha(t - t')}\right) \tag{3}$$

where $G(\vec{r}, \vec{r}', t, t')$ is the well known Green's function.

It is convenient to define the three following expressions:

$$G_X(x, t, t') = \frac{1}{[\pi\alpha(t - t')]} \exp\left(\frac{-x^2}{4\alpha(t - t')}\right)$$

$$G_Y(y, t, t') = \frac{1}{[\pi\alpha(t - t')]} \exp\left(\frac{-y^2}{4\alpha(t - t')}\right)$$

and

$$G_Z(z, t, t') = \frac{1}{[\pi\alpha(t - t')]} \exp\left(\frac{-z^2}{4\alpha(t - t')}\right). \tag{4}$$

Then, the solution of the equation (3) based on the multiplicative property of the Green's function appears as

$$G(\vec{r}, \vec{r}', t, t') = \tfrac{1}{4} G_X(x - x', t, t') G_Y(y - y', t, t') \times G_Z(z - z', t, t'). \tag{5}$$

If the point source delivers a power density I, from $t = 0$ up to the time t, then the increase of the enthalpy becomes

$$\Delta H(\vec{r}, t) = \int_0^t I G(\vec{r}, \vec{r}', t, t')\,\mathrm{d}t. \tag{6}$$

According to the fact that the laser beam is modelled as a continuum of point sources, the power density can be written as follows:

$$I(x', y', z') = I_0 \times P_X(x') P_Y(y') P_Z(z') \tag{7}$$

where the functions $P_X(x')$, $P_Y(y')$ and $P_Z(z')$ characterize the spatial distribution of the beam along the three coordinates x, y and z, respectively.

Substituting (5) and (7) in (6), we obtain

$$\Delta H(\vec{r}, t) = \int_0^t \int_{-\infty}^{+\infty} \int_{-\infty}^{+\infty} \int_{-\infty}^{+\infty} \frac{I_0}{4} P_X(x') \times G_X(x - x', t, t') \times P_Y(y') \times G_Y(y - y', t, t') \times P_Z(z') \times G_Z(z - z', t, t')\,\mathrm{d}x'\,\mathrm{d}y'\,\mathrm{d}z'\,\mathrm{d}t'. \tag{8}$$

Table 1. Numerical values of the parameters of energy distribution in the laser beam–material interaction plane.

i	1	2	3	4	5
x'_{0i} (μm)	0	0	125	295	−280
y'_{0i} (μm)	91	−91	0	0	150
r_{0i} (μm)	250	250	100	90	1200
P_i (10^{-2})	10.1	10.1	4.4	4.8	70.5

This equation can be expressed in a more concise way using the products of convolution

$$\Delta H(\vec{r}, t) = \frac{I_0}{4}\int_0^t (P_X \otimes G_X)(x)(P_Y \otimes G_Y)(y)(P_Z \otimes G_Z)(z)\,\mathrm{d}t'. \quad (9)$$

Consider now the following.

(i) The multi-pulse irradiation sequence, characterized by the pulse duration, τ, and the pulse repetition rate, f, through the time dependence function $\chi(t)$

$$\chi(t) = \sum_{n'=0}^{\infty}\left\{\pi_\tau \otimes \delta\left[t'' - \left(\frac{n'}{f} + \frac{\tau}{2}\right)\right]\right\} = \sum_{n'=0}^{\infty}\int_0^{+\infty}\pi_\tau(t'') \times \delta\left[(t - t'') - \left(\frac{n'}{f} + \frac{\tau}{2}\right)\right]\mathrm{d}t'' \quad (10)$$

where π_τ is a function being one within the time range $[-\tau/2, +\tau/2]$ and zero elsewhere and δ is Dirac's distribution.

(ii) The shape of the laser beam energy distribution described as a theoretical fashion by two Gaussian distributions, along both the x and y axes, and by a Dirac's distribution along the depth z ($P_z(z') = \delta(z')$)

$$I(x', y', z') = I_0 \exp\left(-\frac{x'^2 + y'^2}{r_0^2}\right)\delta(z') \quad (11)$$

where I_0 is the radiant exposure and r_0 is the radius of the laser beam, satisfying the conservation of pulse energy E as follows

$$\int_0^\tau\int_{-\infty}^{+\infty}\int_{-\infty}^{+\infty}\int_{-\infty}^{+\infty} I_0 \times \exp\left(-\frac{x'^2 - y'^2}{r_0^2}\right)\delta(z')\,\mathrm{d}x'\,\mathrm{d}y'\,\mathrm{d}z'\,\mathrm{d}t' = E. \quad (12)$$

This yields

$$I_0 = \frac{E}{\tau}\frac{1}{\pi r_0^2}. \quad (13)$$

Thus, using (9), (10) and (13), the solution available for a beam moving along x at a constant velocity V is

$$\Delta H(\vec{r}, t) = \frac{E}{4\tau}\frac{1}{\pi r_0^2}\int_0^t\left(\frac{\chi(t')}{[\pi\alpha(t - t')]^{3/2}} \times \exp\left(-\frac{z^2}{4\alpha(t - t')}\right)\int_{-\infty}^{+\infty}\exp\left(-\frac{x'^2}{r_0^2}\right) \times \exp\left(-\frac{[x - (x' + Vt')]^2}{4\alpha(t - t')}\right)\mathrm{d}x'\int_{-\infty}^{+\infty}\exp\left(-\frac{y'^2}{r_0^2}\right) \times \exp\left(-\frac{[y - y']^2}{4\alpha(t - t')}\right)\mathrm{d}y'\right)\mathrm{d}t'. \quad (14)$$

Integrating with respect to x' and y' from $-\infty$ up to $+\infty$ gives the following results:

$$\int_{-\infty}^{+\infty}\exp\left(-\frac{x'^2}{r_0^2}\right)\exp\left(-\frac{[x - (x' + Vt')]^2}{4\alpha(t - t')}\right)\mathrm{d}x' = \frac{\pi^{1/2}(4\alpha r_0^2(t - t'))^{1/2}}{(4\alpha(t - t') + r_0^2)^{1/2}}\exp\left(-\frac{(x - Vt')^2}{4\alpha(t - t') + r_0^2}\right) \quad (15)$$

and

$$\int_{-\infty}^{+\infty}\exp\left(-\frac{y'^2}{r_0^2}\right)\exp\left(-\frac{[y - y']^2}{4\alpha(t - t')}\right)\mathrm{d}y' = \frac{\pi^{1/2}(4\alpha r_0^2(t - t'))^{1/2}}{(4\alpha(t - t') + r_0^2)^{1/2}}\exp\left(-\frac{y^2}{4\alpha(t - t') + r_0^2}\right). \quad (16)$$

Substituting (15) and (16) into (14), we obtain finally

$$\Delta H(\vec{r}, t) = \frac{AE}{\tau\pi^{3/2}\alpha^{1/2}}\int_0^t\left[\chi(t')\exp\left(-\frac{z^2}{4\alpha(t - t')}\right) \times \exp\left(-\frac{(x - Vt')^2 + y^2}{4\alpha(t - t') + r_0^2}\right)\right] \times\{(t - t')^{1/2}[4\alpha(t - t') + r_0^2]\}^{-1}\,\mathrm{d}t' \quad (17)$$

where A is an apparent absorption coefficient taking into account the complex interaction between the laser beam and the surface of the moving target.

The complex energy distribution of the laser beam actually used in our investigations is well described by a sum of n Gaussian distributions which are centred on the coordinates x'_{0i}, y'_{0i} according to the radius r_{0i} and the relative intensity P_i. From the following relationship

$$\int_0^\tau\int_{-\infty}^{+\infty}\int_{-\infty}^{+\infty}\int_{-\infty}^{+\infty} P(x', y', z')\delta(z')\,\mathrm{d}x'\,\mathrm{d}y'\,\mathrm{d}z'\,\mathrm{d}t' = E \quad (18)$$

we obtain

$$P(x', y', z') = \sum_{i=1}^{n}\left[\frac{P_i E}{\pi\tau r_{0i}^2(\sum_{j=1}^{n} P_j)} \times \exp\left(-\frac{(x' - x'_{0i})^2 + (y' - y'_{0i})^2}{r_{0i}^2}\right)\right]. \quad (19)$$

This yields, from equation (17),

$$\Delta H(\vec{r}, t) = \frac{AE}{\tau\pi^{3/2}\alpha^{1/2}(\sum_{j=1}^{n} P_j)}\sum_{i=1}^{n}\left\{P_i\int_0^t\left[\chi(t') \times \exp\left(-\frac{z^2}{4\alpha(t - t')}\right) \times \exp\left(-\frac{(x - (x'_{0i} - Vt'))^2 + (y - y'_{0i})^2}{4\alpha(t - t') + r_0^2}\right)\right] \times\{(t - t')^{1/2}[4\alpha(t - t') + r_{0i}^2]\}^{-1}\,\mathrm{d}t'\right\}. \quad (20)$$

An accurate representation of the space energy distribution exhibited by the laser beam used was indispensable to ensure reliable thermal modelling. The one-pulse irradiation of photosensitive surfaces showed that the energy distribution in the laser beam–material interaction plane could be divided into five Gaussian distributions, the parameters of which are given in table 1. The actual optical absorption coefficient, A_R, is dependent on the temperature. This coefficient is therefore dependent on the time and the space variables x and y.

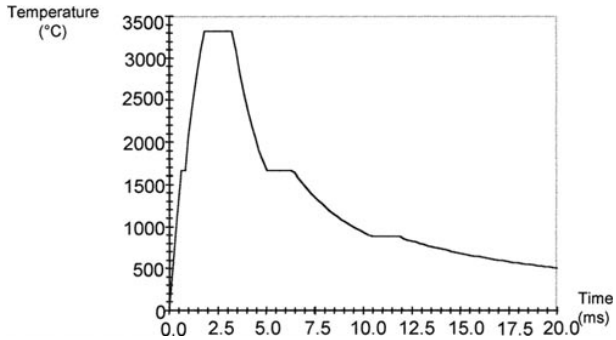

Figure 2. Simulated temperature against time during and after one-pulse irradiation. 50 μm under the focal plane and on the optical axis of the laser beam and with a pulse energy of 3.0 J and pulse duration of 2.7 ms.

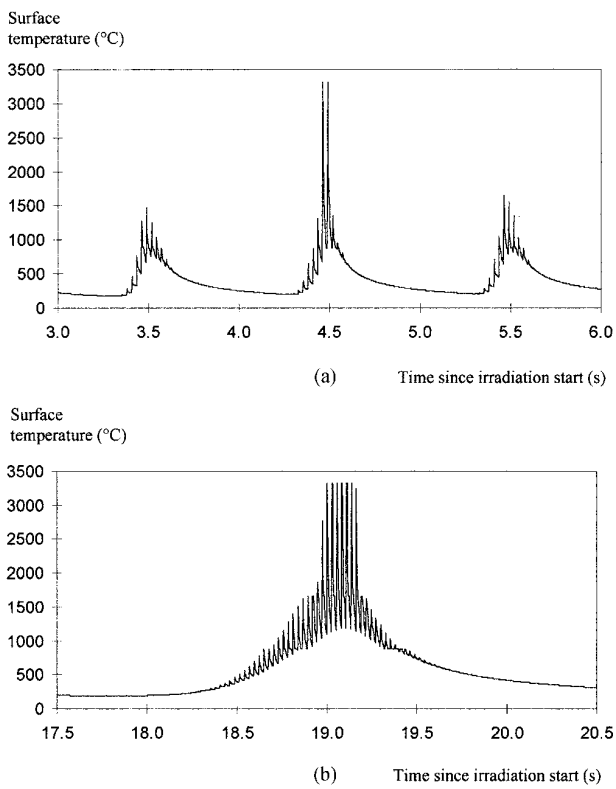

Figure 3. Simulated temperature against time at the surface for two different irradiation treatments: (a) irradiation with a small superposition ratio (R1B1F2P2) and (b) irradiation with a large superposition ratio (R2B1F2P2).

The variation laws of such a coefficient being unknown it was necessary to substitute the apparent absorption coefficient, A, used in the analytical expression, (20), of the thermal modelling. The value $A \approx 0.75$ was previously deduced from the comparison between measured and simulated depths of the molten zone and heat-affected zone, within the range of the irradiation parameter [29].

2.2. Numerical simulation

The different simulations are computed using codes programmed in Turbo Pascal. These programs allow one to simulate a spatio-temporal field of temperatures along one axis or in a plane. They also allow one to evaluate, by three-dimensional simulation, the depths reached by molten zone and the heat-affected zone either after one pulse or after multi-pulse irradiations, with or without beam scanning. Other programs allow one to simulate the moving velocities of the melting or solidification fronts and also the temperature gradients.

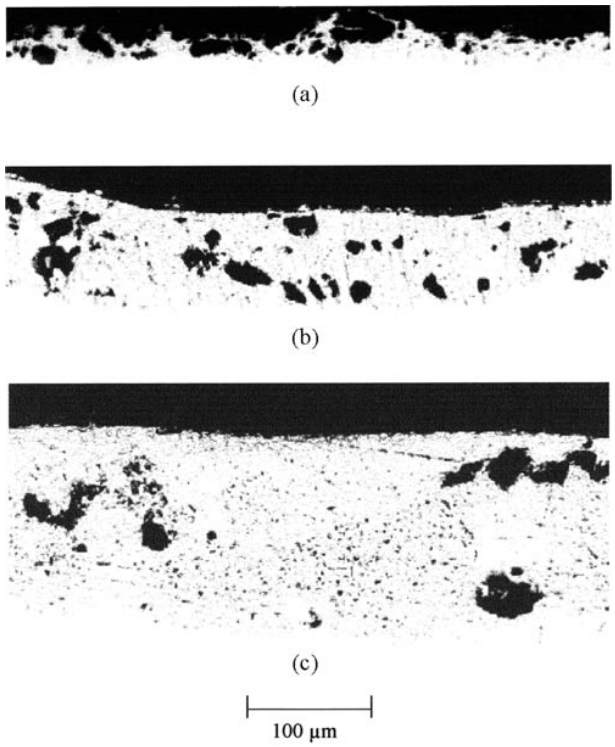

Figure 4. Graphite inclusions in the molten zone in the case of (a) irradiation treatment R2B2F2P1, (b) irradiation treatment R2B1F1P1 and (c) irradiation treatment R2B1F2P1.

3. Results and discussion

The spatio-temporal distribution of temperatures in the irradiated titanium was computed by means of expression (20) and the enthalpy–temperature law which characterizes the metallic titanium. The curve used, $\Delta H(T)$, takes into account the specific heats for the solid and liquid states, and also the latent heats for the allotropic transformation, melting and vaporization of the titanium [31]. On the other hand, the chemical reaction Ti + C $\rightarrow$ TiC only occurs when titanium is in the liquid state because the contact between carbon and titanium, before melting, is very limited. For treatments leading to a molten zone without graphite inclusions, the percentage of carbon incorporated is about 10 at% so we can consider that in all cases 10–15% of the titanium is involved in the reaction Ti + C $\rightarrow$ TiC. The amount of energy necessary to perform this reaction is negligible compared to the energy used to melt 100% of the titanium atoms that are in the molten zone. This justifies the fact that our model does not consider the formation enthalpy of TiC. The temporal evolution of temperature at a point of the titanium during and after one pulse of irradiation is plotted in figure 2. The Simpson's numerical method is used to compute the time integral in expression (20). For numerical considerations, the integral

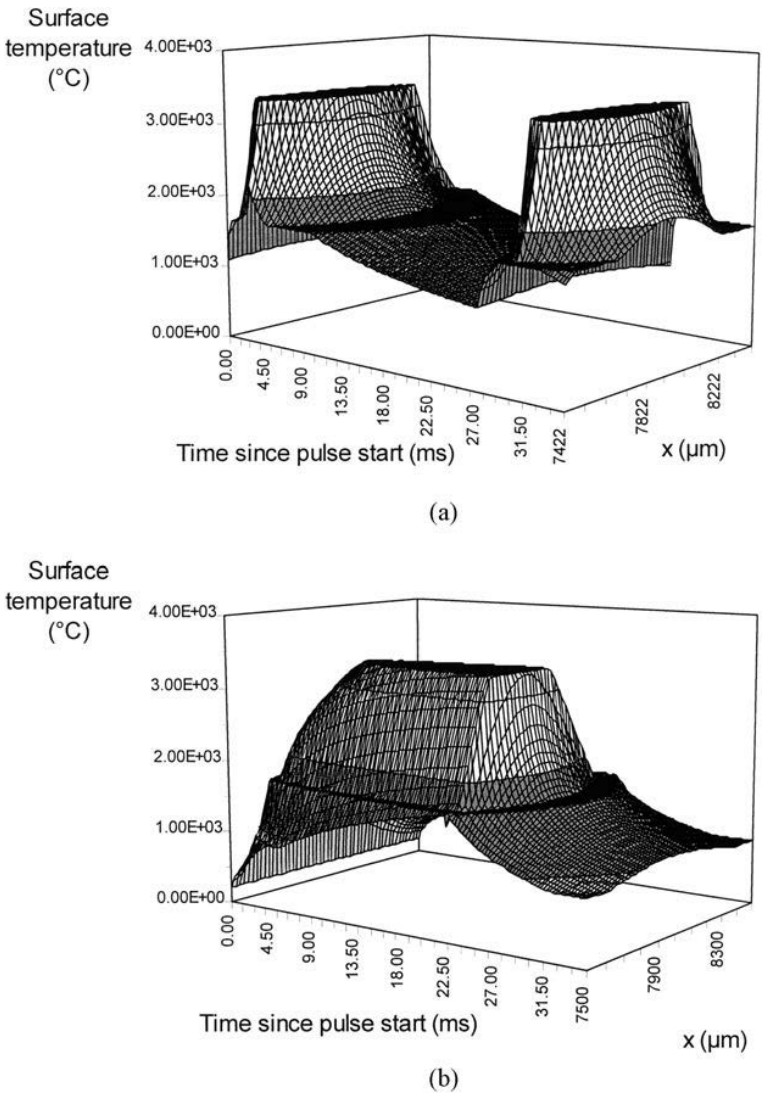

Figure 5. Simulated evolution of the surface temperature against time along the main scanning direction of the laser beam (X axis) during multi-pulse irradiation: using irradiation treatment (a) R2B1F2P2 and (b) R2B1F2P1. The high surface temperatures explain the lack of graphite inclusions after solidification.

of the sum in expression (20) must be replaced by a sum of integrals on the intervals for which the function χ is not equal to zero.

3.1. Irradiation conditions

The diagram of the experimental procedure of surface melting by laser irradiation is depicted in figure 1. Graphite powder suspended in an alcohol and water solution is laid on the sample surface. After evaporation of the liquid solution in an hot-air steam cabinet, the quantity of deposited carbon is checked by weighing. In all cases the graphite powder layer covering the titanium sample was always 20 ± 3 μm thick. Four relevant parameters were considered in carrying out the irradiation treatments. These parameters control the heat transfer through the irradiated material and are dependent on the operative parameters [29]. Two relevant parameters characterize each laser pulse: the surface density of deposited energy, F, and the pulse power, P. Two other parameters describe the pulse succession: the time ratio of laser emission, B, and the superposition ratio of two areas successively irradiated, R. The different irradiation treatments carried out for this study are summarized in table 2.

3.2. Carbon incorporation

The important role played by the superposition ratio was experimentally examined. The mean mass percentage of incorporated carbon was $62.9 \pm 9.6\%$ with a high superposition ratio, of two successively irradiated areas ($R2 = 0.9$) whereas it was only $27.0 \pm 9.9\%$ with a lower superposition ratio ($R1 = 0.5$). This behaviour is elucidated from the simulated evolutions of surface temperature computed on the centre of the treated area for the superposition ratios $R1$ and $R2$ (figure 3). The slower temperature increase due to larger superposition reduces the carbon losses by projection resulting from the expansion of gases trapped between graphite powder grains. The incorporation of carbon is therefore proved to be more efficient with large superpositions of areas successively irradiated.

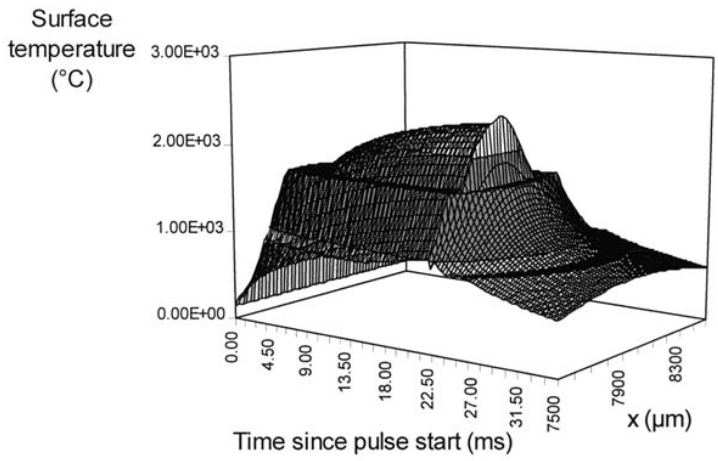

(a)

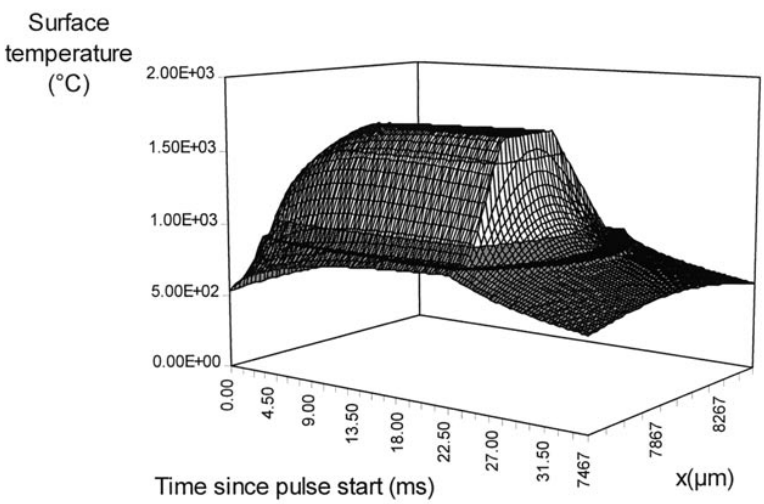

(b)

Figure 6. Simulated evolution of surface temperature against time along the main scanning direction of the laser beam (X axis) during multi-pulse irradiation: using irradiation treatment (a) R2B1F1P1 and (b) R2B2F2P1. The low surface temperatures explain the presence of graphite inclusions after solidification.

Table 2. Experimental conditions of laser irradiation. Relationships between the irradiation treatment, relevant parameters and operative parameters.

	Relevant parameters				Operative parameters			
Irradiation treatment	R	B	F (J mm^{-2})	P (W)	E (J)	τ (ms)	f (s^{-1})	V (mm s^{-1})
R2B1F1P2	0.89 ± 0.04	0.100 ± 0.006	4.6 ± 0.4	$1.11 \times 10^3 \pm 0.11 \times 10^3$	3.0 ± 0.2	2.7 ± 0.1	37.0 ± 0.7	3.78
R2B1F2P2	0.89 ± 0.04	0.100 ± 0.006	5.9 ± 0.4	$1.41 \times 10^3 \pm 0.14 \times 10^3$	3.8 ± 0.2	2.7 ± 0.1	37.0 ± 0.7	3.78
R2B1F1P1	0.89 ± 0.04	0.099 ± 0.002	7.7 ± 0.5	$2.22 \times 10^2 \pm 0.15 \times 10^2$	5.0 ± 0.3	22.5 ± 0.1	4.4 ± 0.1	0.45
R2B1F2P1	0.89 ± 0.04	0.099 ± 0.002	12.4 ± 0.4	$3.56 \times 10^2 \pm 0.25 \times 10^2$	8.0 ± 0.5	22.5 ± 0.1	4.4 ± 0.1	0.45
R2B2F2P1	0.88 ± 0.04	0.50 ± 0.01	3.6 ± 0.2	$1.11 \times 10^2 \pm 0.08 \times 10^2$	2.5 ± 0.2	22.5 ± 0.1	22.0 ± 0.4	2.47
R2B2F2P2	0.88 ± 0.04	0.50 ± 0.01	5.4 ± 0.2	$1.64 \times 10^2 \pm 0.11 \times 10^2$	3.7 ± 0.2	22.5 ± 0.1	22.0 ± 0.4	2.47

3.3. Formation of graphite inclusions

Among the irradiation treatments with high superposition ratios ($R2 = 0.9$), treatments R2B1F1P2 and R2B1F2P2 generated molten zones without graphite inclusions. In contrast, 7% of the molten zone generated by the treatment R2B1F2P1 is composed of graphite inclusions that are 28 μm in mean diameter. In case of treatment R2B1F1P1, the inclusions are 16 μm in mean diameter and compose 14% of the molten zone and in case of the treatments R2B2F2P1 and R2B2F2P2 this percentage increase up to 53% and the diameter of inclusions decreases to 10 μm (table 2, figure 4). These graphite inclusions give much technological importance to such irradiation treatments of titanium. In fact, it was

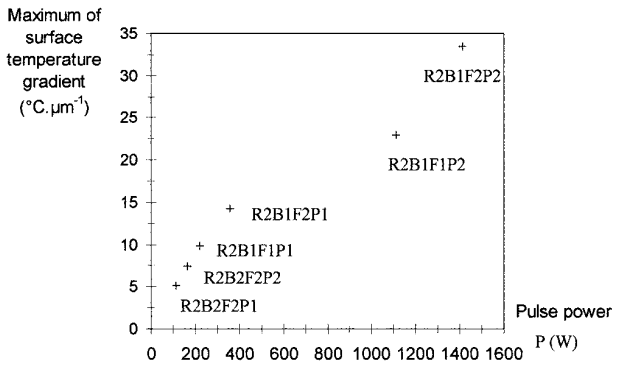

Figure 7. Maxima of the surface temperature gradient computed for various irradiation treatments.

proved in a previous paper [32] that the process of titanium carburization by laser melting allowed the synthesise of a self-lubricating composite coating. Such a coating exhibited a weak friction coefficient by sliding on ceramic (∼0.25) owing to its graphite inclusions as a solid lubricant.

The time evolutions of the temperature along beam scanning axis X (figure 5) justify the proposal that the molten zones in which the surface temperature reaches the vaporization temperature of titanium (3318 °C) contain very few inclusions after the irradiation treatments R2B1F2P2 and R2B1F2P1. This high temperature intensifies the dissolving of carbon in liquid titanium and therefore allows the formation of a larger amount of titanium carbide in the molten zone during its solidification.

The surface temperature remains under 2500 °C (figure 5) during irradiation treatment R2B1F1P1 and the obtained molten zone contains more numerous graphite inclusions. This temperature does not exceed 2000 °C (figure 6) during treatment R2B2F2P1 or R2B2F2P2 and the molten zone contains very numerous inclusions.

During all these irradiation treatments, a more or less large volume ratio of graphite is dissolved in liquid titanium to form some further titanium carbide during the primary solidification. The amount of carbide is reduced by the slower dissolution of graphite in liquid titanium at a lower temperature and by a shorter life time of molten bath. A larger amount of non-dissolved graphite, under the state of inclusions in the molten zone after its solidification, results from the lower temperature reached by the molten titanium bath.

Our thermal modelling does not take into account the convection flows in the molten bath. Nevertheless the simulations allow us to estimate the importance of the Marangoni's effect, which the flow is proportional to the surface temperature gradient on the molten bath. These maximum temperature gradients along beam scanning axis X are computed for various irradiation treatments and are given against the pulse power, P, in figure 7. The treatments with the most intense convection flows generate the smallest number of graphite inclusions in the molten zone. Such flows during titanium melting disperse the graphite powder in the bath and intensify the dissolution of carbon in the liquid titanium.

3.4. Solidification structures

Two typical microstructures were solidified in molten zone according to the irradiation treatments. Titanium carbide

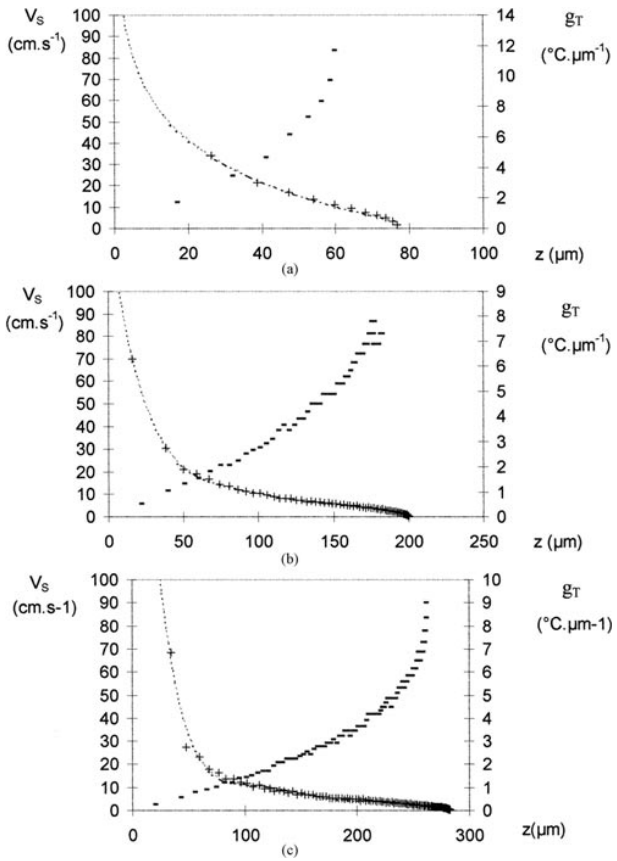

Figure 8. Propagation velocities of solidification front V_s (+) and temperature gradients ahead solidification front g_T (−) against the depth of melted bath, Z, computed for various irradiation treatments: (a) R2B2F2P2, (b) R2B1F2P1 and (c) R2B1F2P2.

enclosed in the metallic titanium matrix was either in a state of cellular dendrites or in a state of globular grains.

The computations of the velocity of the solidification front, V_S, justify the lack of structures resulting from very fast solidifications and which are very out of equilibrium. First the melting front advances up to an area in which a maximum depth extends to two or three hundreds micrometres prior to its velocity becomes zero. Then, the solidification starts from the boundary of molten bath when the cooling begins. The solidification front accelerates from zero velocity to reach several tens of centimetres per second close to the surface. The fastest solidification velocity given by our simulations is only 70 cm s^{-1} (figure 8). It is impossible to simulate the solidification velocity for the distances less than about 20 μm from the surface ($z < 20$ μm) because of the necessary time increments, which become too much short. It is generally necessary that alloys solidify with velocities, V_S, higher than 1 m s^{-1} in order to generate structures which are very out of equilibrium [33]. Propagation velocity extrapolation gives values more than 1 m s^{-1} close to the surface, but the thermal surface losses by conduction, convection and radiation become non-negligible. The highest simulated speeds of the solidification front are located near the surface along an axis normal to the centre of the molten bath (figure 9). Now, this area will melt again during the next pulse, whereas the back part of molten zone, where the solidification velocities are significantly lower, will definitely be solidified.

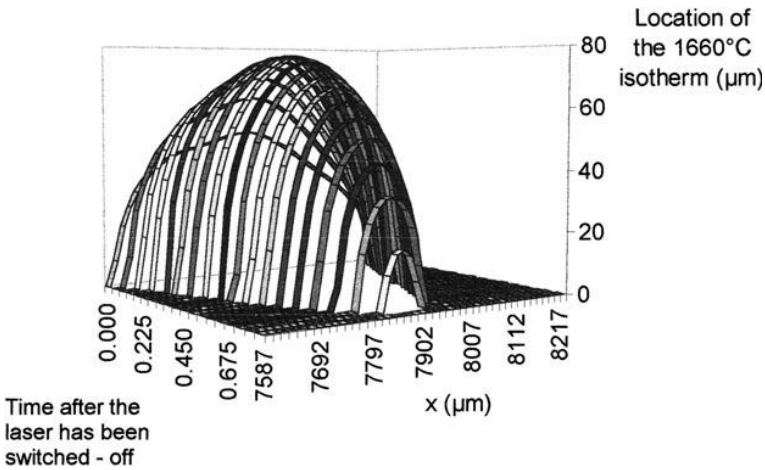

Figure 9. Location of the isotherm 1660 °C (melting temperature of titanium) along the main scanning direction of the laser beam (X axis) and against time. The highest moving speeds of the simulated solidification front are located near the surface along the axis normal to the centre of the molten bath.

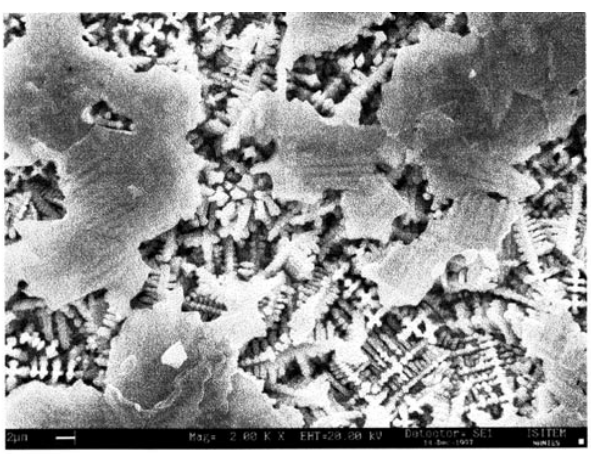

(a)

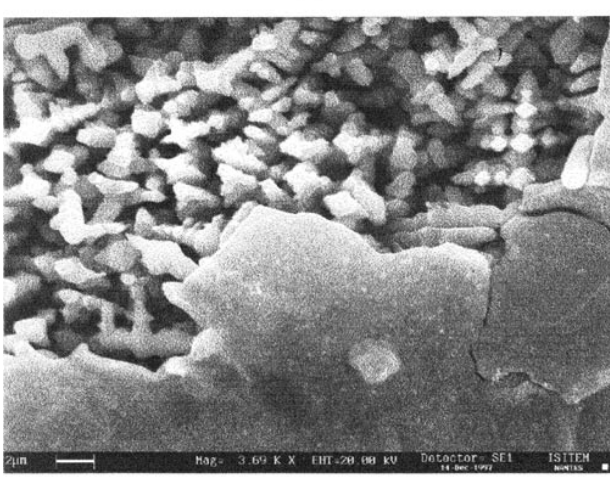

(b)

Figure 10. SEM micrographs of the sample surface after irradiation treatment (a) R2B1F1P2 and (b) R2B1F2P2 and chemical etching. The surface layer (thin plates) of titanium carbide and the underlying dendritic microstructure of this phase are revealed.

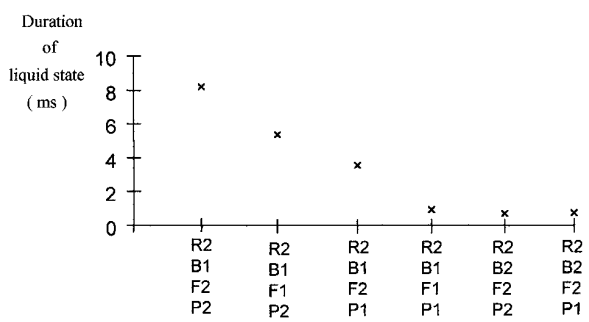

Figure 11. Computed durations of the liquid state just after the laser was switched off for various irradiation treatments. These different durations are necessary for the solidification front to reach the top surface after the end of a pulse.

The microstructure of molten zone is dependent on the circumstances of solidification, which are described by the ratio between the temperature gradient and solidification velocity, g_T / V_S [32]. When the solidification front comes up to the surface of molten bath ($z = 0$), g_T decreases whereas V_S increases. The ratio g_T / V_S during solidification is therefore a decreasing function, on which the morphology of the titanium carbide phase is dependent. Simulated temperature gradients ahead of the solidification front (g_T) and propagation velocities (V_S) are shown in figure 8. The drastic decrease of the ratio g_T / V_S from the outset of solidification can explain why the characteristic morphology, resulting from the plane-front growth due to very strong ratios in bottom of the molten zone, was never observed. The deep zone of the plane-front growth of the solidification structure was therefore very thin and not noticeable.

The morphology and size of the solidification microstructures are dependent on the local physicochemical conditions which exist on short spatio-temporal scales. The prediction of such microstructures requires an exact knowledge of the temperature field and the concentration gradient of the dissolved element (carbon in the present case) near the solidification front [34–36]; this last feature is unknown. On the other hand, a multiplicity of melting–solidification cycles can result from pulsed irradiation (figure 4) and induce more complex processes of microstructure growth.

3.5. Surface plane-front growth

The surface of carburized titanium is resistant to Krool's etching solution after the irradiation treatments R2B1F1P2 and R2B1F2P2. This reagent etches metallic titanium, a surface layer 1 μm thick observed by SEM (figure 10) was therefore a non-metallic phase. On the one hand, x-ray diffraction executed before the etching treatment did not detect oxides. On the other hand, analysis by electron microprobe (EDS) showed that such a surface layer was only made up of carbon and titanium. It is deduced that titanium carbide was solidified by plane-front growth from the surface of molten bath, before the other solidification front, which starts from the bottom of bath, reached the surface. Oxidation of each sample was prevented by an argon stream directed onto the irradiation zone, the flow rate of which was 10 l min^{-1}. This solidification process is proved by thermal simulation. In fact, the computations for irradiation treatments R2B1F2P2 and R2B1F1P2 give the longest durations of the liquid state since the end of last pulse (figure 11), i.e. the longest durations necessary for the solidification front to reach the top surface.

4. Conclusions

The simulation of the spatio-temporal temperature distribution in the material during its irradiation treatment allows us to describe or predict the thermal effects and the structural modifications generated by the pulsed laser irradiation. We propose a semi-analytical modelling because of the failure to appreciate the heat flux absorbed at each surface point and in order to obtain shorter computation times. This modelling is founded on the resolution of a differential equation by means of Green's functions and it takes into account the pulsed nature of the irradiations which are carried out. Moreover, it also takes into account the enthalpy variations which are associated with the isotherm transformations of the metal: allotropy, melting and vaporization. The temperature fields within the irradiated material are simulated for different times owing to the calculus of the integral on the time variable by the numerical method.

The thermal simulation of the process of surface melting with the carburization of titanium by pulsed laser irradiation allows us to better interpret the structural states of the molten zone obtained after solidification. Such a simulation also makes easier the optimization of the operative parameters for this process of surface hardening, with or without the incorporation of lubricating graphite inclusions and with a view to carry this out for a number of technological applications.

Acknowledgments

The authors are very grateful to E Geffriaud and M-J Moya, and also to M-G Robert for her technical assistance.

References

[1] Ettaqi S *et al* 1995 Structural study of a titanium/titanium boride cermet coating formed upon laser fusion of boron on a titanium foil *J. Mater. Chem.* **11** 1905–8

[2] Ettaqi S *et al* 1998 Mechanical, structural and tribological properties of titanium nitrided by a pulsed laser *Surf. Coat. Technol.* **100–101** 428–32

[3] Wu P, Zhou C Z and Tang X N 1995 Laser alloying of a gradient metal–ceramic layer to enhance wear properties *Surf. Coat. Technol.* **73** 111–14

[4] Anjos M A *et al* 1995 Fe–Cr–Ni–Mo–C alloys produced by laser surface alloying *Surf. Coat. Technol.* **70** 235–42

[5] Wang M and Wu W 1995 Microstructure of laser-surface alloyed cast iron with Cr–Al–Y alloy *Surf. Coat. Technol.* **72** 181–8

[6] Carvalho P A and Vilar R 1996 Laser alloying of zinc with aluminium: solidification structures *Surf. Coat. Technol.* **91** 158–66

[7] Kou S 1982 Welding, glazing and heat treating—a dimensional analysis of heat flow *Metall. Trans.* A **13** 363–71

[8] Rappaz M *et al* 1986 Solidification front and growth rate during laser remelting *Proc. Laser Treatment of Materials, Eur. Conf. (Bad Nauheim, Germany)*

[9] Lax M 1977 Temperature rise induced by a laser beam *J. Appl. Phys.* **48** 3919–24

[10] Cline H E and Anthony T R 1977 Heat treating and melting material with a scanning laser or electron beam *J. Appl. Phys.* **48** 3815–900

[11] Nissim Y I *et al* 1980 Temperature distributions produced in semiconductors by a scanning elliptical or circular cw laser beam *J. Appl. Phys.* **51** 274–9

[12] Shercliff H R and Ashby M F 1991 The prediction of case depth in laser transformation hardening *Metall. Trans.* A **22** 2459–65

[13] Rykalin N N, Uglov A A and Kokora A 1978 *Laser Machining and Welding* (Oxford: Pergamon) ch 3

[14] Hu C and Baker T N 1995 Prediction of laser transformation hardening depth using a line source model *Acta. Metall. Mater.* **43** 3563–9

[15] Bahtaoui C and L'Huillier J P 1996 Modelling of pulsed laser heating of metallic coating on substrate: action of typical laser pulse shape *MAT-TEC* 63–9

[16] Tokarev V N and Kaplan A F H 1999 An analytical modelling of time dependent pulsed laser melting *J. Appl. Phys.* **86** 2836–46

[17] Shneidman V A 1996 Interplay of latent heat and time-dependent nucleation effects following pulsed-laser melting of a thin silicon film *J. Appl. Phys.* **80** 803–11

[18] Wood R F, Geist G A and Liu C L 1996 Two-dimensional modelling of a pulsed-laser irradiated alpha-Si and other materials *Phys. Rev.* B **53** 15 863–70

[19] Carlaws H S and Jaegger J C 1959 *Conduction of Heat in Solids* (Oxford: Clarendon)

[20] Hsu S C, Chakravorty S and Mehrabian R 1978 Rapid melting and solidification of a surface layer *Metall. Trans.* B **9** 221–9

[21] Hsu S C, Kou S and Mehrabian R 1980 Rapid melting and solidification of a surface due to a stationary heat flux *Metall. Trans.* B **11** 29–38

[22] Bing-Wu Gu *et al* 1994 Three dimensional numerical model for laser transformation hardening of metals *Meas. Sci. Technol.* **10** 425–30

[23] Bahtaoui C 1995 Contribution à la modélisation du comportement thermique des composites chrome/aluminium et nickel/acier 1018 soumis à des flux lasers impulsionnels: les transferts de matière induits *Thesis* ENSAM, France

[24] Chan C L, Mazumder J and Chen M M 1987 Three-dimensional axisymmetric model for convection in laser-melted pools *Meas. Sci. Technol.* **3** 306–11

[25] Kreutz E W and Pirch N 1991 Melt dynamics in surface processing with laser radiation: calculations and applications *Laser de puissance et traitements de matériaux* (Lausanne, Switzerland: Presses Polytechniques et Universitaires Romandes) pp 535–55

[26] Chan C, Mazumder J and Chen M M 1984 A two-dimensional transient model for convection in laser melted-pool *Metall. Trans.* A **15** 2175–84

[27] Basu B and Srinivasan J 1988 Numerical study of steady-state laser melting problem *Int. J. Heat Mass Transfer.* **31** 2331–8

[28] Galerie A, Pons M and Caillet M 1987 Elaboration d'alliages de surface sous irradiation laser *Meas. Sci. Technol.* **88** 127–34
[29] Courant B, Hantzpergue J J and Benayoun S, Structure of titanium surfaces carburized by pulsed laser melting with graphite addition, submitted
[30] Schriempf S T, Stegman R L and Nash G E 1973 *IEEE J. Quantum Electron.* **9** 648
[31] Courant B, Ettaqi S, Fouilland-Paillé L, Benayoun S and Hantzpergue J J *Proc. 11th Int. Conf. on the Surface Modification Technologies, SMT 11 (Paris, France)*
[32] Courant B, Hantzpergue J J and Benayoun S 1999 Surface treatment of titanium by laser irradiation to improve resistance to dry-sliding friction *Wear* **236** 39–46
[33] Vannes A B and Langlade-Bomba C 1998 Les lasers de puissance: un vecteur idéal pour réaliser des traitements superficiels? *Proc. 'Avancées des traitements et revêtements de surfaces', Section Régionale Ouest de la SF2M* (Angers, France: ENSAM)
[34] Kurz W and Fisher D J 1986 *Fundamentals of Solidification* (Switzerland: Transtech)
[35] Lasalmonie A and Duflos F 1988 Les paramètres de la solidification rapide. Solidification des alliages (du procédé à la microstructure) *Ecole d'été Carry-le-Rouet* ed F Durand, pp 313–27
[36] Paidassi S 1988 Le traitement de fusion superficielle (TFS). Solidification des alliages (du procédé à la microstructure) *Ecole d'été Carry-le-Rouet* ed F Durand, pp 341–56